Advances in Computational Mathematics (2023) 49:45
https://doi.org/10.1007/s10444-023-10046-y

Fast and accurate solvers for simulating Janus particle suspensions in Stokes flow

Ryan Kohl[1] · **Eduardo Corona**[2] · **Vani Cheruvu**[3] · **Shravan Veerapaneni**[1]

Received: 29 August 2022 / Accepted: 2 May 2023 / Published online: 23 June 2023

Abstract

We present a novel computational framework for the simulation of rigid spherical Janus particle suspensions in Stokes flow. For a wide array of Janus particle types, we show long-range interactions may be resolved using fast, spectrally accurate boundary integral methods. We incorporate this to our rigid body Stokes platform, which resolves hydrodynamic interactions and contact. Our approach features the use of spherical harmonic expansions for spectrally accurate integral operator evaluation, complementarity-based collision resolution, and optimal $\mathcal{O}(n)$ scaling with the number of particles when accelerated via fast summation techniques. We demonstrate the versatility of our simulation platform through three test cases involving Janus particle systems prominent in applications: *amphiphilic, bipolar electric* and *phoretic* particles. For each test case, we formulate Janus particle interactions in boundary integral form and use our framework to demonstrate examples of self-assembly and complex collective behavior characteristic of these systems.

Keywords Janus particles · Boundary integral methods · Fast multipole methods

Mathematics Subject Classification (2010) 65N80

Communicated by: Silas Alben

✉ Eduardo Corona
eduardo.corona@colorado.edu

[1] Department of Mathematics, University of Michigan, Ann Arbor, USA

[2] Department of Applied Mathematics, University of Colorado at Boulder, Boulder, USA

[3] Department of Mathematics and Statistics, University of Toledo, Toledo, USA

1 Introduction

The term "Janus particle" originated from the synthesis of two-faced spheres with amphiphilic structure like that of the phospholipid components of cell membranes. It is now, however, applied to a wide class of colloidal particles with more than a single type of surface chemistry or composition. The anisotropic structure in most Janus particles involves two hemispheres that differ in electric, magnetic or optical properties or in their physicochemical interaction with the surrounding fluid. Dense suspensions of Janus particles have been widely demonstrated to display complex aggregate behavior, clustering and self-assembly into larger-scale structures [1–3]. Spurred by advances in design and manufacturing, the study of self-assembling materials based on Janus particle suspensions has garnered great interest, showing particular potential in biomedical applications such as drug delivery, medical imaging and manufacturing of biosensors and micromotors [4–6].

In the study of dense particulate systems, direct numerical simulation (DNS) can play a crucial role to gain insight into their complex behavior and make accurate predictions. DNS of such systems, however, requires overcoming several challenges: methods must accurately resolve short-ranged interactions (e.g., collisions) as well as computationally intensive long-ranged, many-body interactions (e.g., hydrodynamic). Due to slow relaxation times and non-linearity typical of soft matter systems, robust and scalable solvers are required to tackle the long-term simulations involved.

Furthermore, DNS of Janus particle suspensions epitomizes the demanding nature of multiphysics systems. The dynamics of Janus particle suspensions result from the coupling of one or several long-range physicochemical fields with the fluid flow. At particle surfaces, boundary conditions such as surface traction balance, induced fluid slip, and electromagnetic field jump conditions must be accurately satisfied. Additional coupling can occur in the bulk, for instance, due to advection of chemical solutes. Since self-assembly and clustering are the key phenomena of interest, resolving particle collisions and confinement effects are unavoidable.

In part owing to these challenges, DNS studies of the hydrodynamics of Janus particle suspensions are rather scarce; fluid dynamics of a moderate number of particles have been studied in two [7–11] and three spatial dimensions [12], while large-scale simulation studies have focused on statistical molecular simulation methods such as Molecular Dynamics, Lattice Boltzmann and Monte Carlo methods [13–15]. In this work, we seek to bridge this gap and propose an efficient, fast algorithmic framework for DNS of dense Janus suspensions in three dimensions, building on recent advances in the state-of-the-art rigid body Stokes solvers.

With regard to DNS of rigid particle suspensions, a number of numerical methods have been developed in the past few decades; They may be classified according to how they resolve hydrodynamic particle interactions and near-field lubrication effects. These include approximation methods such as Rotne-Prager-Yamakawa [16], Stokesian dynamics [17] and multipole methods [18], as well as schemes that directly solve the underlying partial differential equation (PDE) such as fictitious domain methods, immersed boundary methods and boundary integral methods [19]. In the context of numerical PDE solution, boundary integral methods are particularly attractive due to dimensionality reduction and improved numerical conditioning. The key numerical

hurdle for effective implementation of these methods is often the fast and accurate evaluation of boundary layer potentials. Overcoming this hurdle, recent contributions in this field have led to the implementation of large-scale simulation platforms for particulate Stokes flow simulation in three dimensions [20–23].

In particular, a scalable computational framework adaptable to a large class of the Stokes mobility solvers was proposed in [23] by incorporating a parallel complementarity-based collision resolution algorithm. In addition, a scalable implementation of the spectrally accurate boundary integral method developed in [24] was used to simulate active matter systems of up to $\mathcal{O}(10^5)$ particles. This method combines spectral analysis in spherical harmonics bases to perform fast singular and near-singular evaluation of Laplace and Stokes potentials, and fast multipole methods to compute long-range interactions.

Our contributions in this work to the study of Janus particles through boundary integral simulations are three-fold. First, we extend the method in [24] for efficient scalar potential evaluation to encompass screened Laplace potentials. Second, we couple our scalar evaluation with our rigid body Stokes solver [23, 25] to explore three-dimensional interactions. Finally, we develop well-conditioned boundary integral formulations for three different types of Janus particles prominent in biomedical and material science research [4], namely, *amphiphilic*, *bipolar* and *phoretic* particles. Amphiphilic particles may be employed to model bilipid membranes in cells and to interact with hydrophobic drug particles. Bipolar and phoretic particles are of interest because their motion can be manipulated, via electromagnetic fields and chemical gradients, respectively [26, 27].

This paper is organized as follows. In Section 2 we discuss the scalar potentials, introducing notation and relevant boundary integral operators. In Section 3, we develop fast, spectrally accurate methods for boundary integral operator (BIO) evaluation. We then discuss the three classes of Janus particles in detail in Sections 4 through 6, demonstrating how the general set of tools we have developed is adapted to each specific problem. For each of these Janus particle test cases, we use our rigid body solver to reproduce well-known collective behavior.

2 Mathematical preliminaries

In this section, we provide the necessary mathematical background for the coupled system of boundary integral equations formulation of Janus and hydrodynamic particle interactions. We present our analysis of the spectra and evaluation formulas for screened Laplace boundary integral operators (BIO)s employed in the evaluation schemes in Section 3.

Notation

In each problem formulation we will consider a system of M rigid spherical Janus particles. For each particle i we adopt the following notation:

We refer to the union of particle interiors and surfaces as $\Omega = \cup_{i=1}^{M} \Omega_i$ and $\Gamma = \cup_{i=1}^{M} \Gamma_i$, respectively. The domain exterior to these particles will be denoted by Ω_∞. For simulations confined in a spherical shell, we denote the surface of the shell by Γ_∞. For unbounded simulations, we have that $\Gamma_\infty = \emptyset$.

particle #	interior	surface	radius
i	Ω_i	Γ_i	r_i
net	net	translational	rotational
force	torque	velocity	velocity
$\boldsymbol{F_i}$	$\boldsymbol{T_i}$	$\boldsymbol{v_i}$	$\boldsymbol{\omega_i}$

2.1 Problem setup

In all cases considered in this work, the Janus interaction potential, which we denote by ϕ, is shown to satisfy a screened Laplace equation,

$$\nabla^2\phi(\boldsymbol{x}) - \lambda^2\phi(\boldsymbol{x}) = 0 \ \ \forall\, \boldsymbol{x} \in \Omega_\infty. \tag{1a}$$

This equation models long-ranged interactions which are damped by the medium. The strength of the damping is controlled by the parameter λ. The quantity $\frac{1}{\lambda}$ has units of length and is typically referred to as the *Debye length*. In models where damping is negligible ($\lambda = 0$), this simplifies to the standard Laplace equation.

The boundary condition at particle surfaces is application-dependent (e.g., Dirichlet, Neumann). If Ω_∞ is unbounded, the potential must also satisfy the decay condition,

$$\lim_{\|\boldsymbol{x}\|\to\infty} \phi(\boldsymbol{x}) = 0. \tag{1b}$$

Janus and hydrodynamic interaction coupling

Coupling between Janus and hydrodynamic particle interactions involves force and torque balance at particle surfaces. Given the Janus interaction potential ϕ, we can compute the associated stress tensor $\mathcal{T}$. In electrostatic applications, for instance, $\mathcal{T}$ is the Maxwell stress, with ϵ_0 denoting vacuum permittivity.

$$\mathcal{T} = \epsilon_0(\nabla\phi \otimes \nabla\phi - \frac{1}{2}\|\nabla\phi\|^2 I). \tag{2}$$

The net force and torque on particle i are then given by

$$\int_{\Gamma_i} (\mathcal{T}\cdot\boldsymbol{\nu})dS_y = \boldsymbol{F_i}, \quad \int_{\Gamma_i} (\boldsymbol{x} - \boldsymbol{x}_i^c) \times (\mathcal{T}\cdot\boldsymbol{\nu})dS_y = \boldsymbol{T_i}, \tag{3}$$

where ν is the outward normal vector to the surface Γ_i. From a computational standpoint, this requires the accurate evaluation of the Janus force field $-\nabla\phi$. This computation is also sufficient in the case of the phoretic model in Section 6, in which a tangential slip velocity induced by chemical activity is involved.

Rigid body Stokes problem

In order to evolve our particulate system, we need to find the rigid body velocities $(\boldsymbol{v}_i, \boldsymbol{\omega}_i)$ which correspond to inter-particle interactions for a given configuration. Given net forces and torques $(\boldsymbol{F}_i, \boldsymbol{T}_i)$ on each rigid body, the problem of solving the Stokes equation to obtain unknown rigid body velocities $(\boldsymbol{v}_i, \boldsymbol{\omega}_i)$ is known as the rigid body

Stokes mobility problem, defined by the system of equations in 4. In this equation, $\boldsymbol{u}$ denotes the Stokes velocity field and p the corresponding pressure. We employ the second-kind boundary integral formulation in [24, 25] to solve this problem.

$$\begin{aligned} -\nabla p + \nabla^2 \boldsymbol{u} &= 0 \quad \text{in} \quad \Omega_\infty, \\ \nabla \cdot \boldsymbol{u} &= 0 \quad \text{in} \quad \Omega_\infty, \\ \lim_{\|\boldsymbol{x}\| \to \infty} \boldsymbol{u} &= 0, \\ \boldsymbol{u} &= \boldsymbol{v}^k + \boldsymbol{\omega}^k \times (\boldsymbol{x} - \mathbf{c}^k) \quad \text{on} \quad \Gamma_k, \quad k = 1, \ldots, M, \\ \int_{\Gamma_k} \boldsymbol{F}\, d\Gamma_k = -\boldsymbol{F}_k \quad &\text{and} \quad \int_{\Gamma_k} (\boldsymbol{x} - \boldsymbol{c}^k) \times \boldsymbol{F}\, d\Gamma_k = -\boldsymbol{T}_k, \quad k = 1, \ldots, M. \end{aligned} \tag{4}$$

In Sections 4 and 5, we input the forces and torques resulting from Janus interactions, as shown in equation (3), into our Stokes mobility problem formulation. We note that our rigid body Stokes computational framework is not specific to the mobility problem, as it may also be adapted to more general prescriptions at the boundary like that of the phoretic Janus particle model in Section 6.

2.2 Boundary integral formulation

We use indirect integral representations of both Janus potential ϕ and velocity field $\boldsymbol{u}$ as combinations of appropriate layer potential boundary integral operators. By design, these representations satisfy the respective PDE and growth conditions. Imposing boundary conditions then yields integral equations for unknown integral densities defined at particle boundaries Γ and geometry boundary Γ_∞.

Screened Laplace layer potentials

For a set λ, let $G_\lambda(\boldsymbol{x}, \boldsymbol{y}) = \frac{1}{4\pi} \frac{e^{-\lambda\|\boldsymbol{x}-\boldsymbol{y}\|}}{\|\boldsymbol{x}-\boldsymbol{y}\|}$ denote the Green's function for the screened Laplace equation. The single- and double-layer potential operators are

$$\mathcal{S}_\lambda[\sigma](\boldsymbol{x}) = \frac{1}{4\pi} \int_\Gamma \frac{e^{-\lambda\|\boldsymbol{x}-\boldsymbol{y}\|}}{\|\boldsymbol{x}-\boldsymbol{y}\|} \sigma(\boldsymbol{y}) d\Gamma, \tag{5a}$$

$$\mathcal{D}_\lambda[\mu](\boldsymbol{x}) = \int_\Gamma \frac{e^{-\lambda\|\boldsymbol{x}-\boldsymbol{y}\|} \boldsymbol{v_y}^T (\boldsymbol{x}-\boldsymbol{y})}{4\pi\|\boldsymbol{x}-\boldsymbol{y}\|} \left(\frac{\lambda}{\|\boldsymbol{x}-\boldsymbol{y}\|} + \frac{1}{\|\boldsymbol{x}-\boldsymbol{y}\|^2} \right) \mu(\boldsymbol{y}) d\Gamma(\boldsymbol{y}). \tag{5b}$$

Formulas for operators $\mathcal{S}'_\lambda$ and $\mathcal{D}'_\lambda$ are included in Appendix B. It is readily seen that for any $\sigma \in L^2(\Gamma)$, $\mathcal{S}_\lambda[\sigma](\boldsymbol{x})$ and $\mathcal{D}_\lambda[\mu](\boldsymbol{x})$ are smooth for $\boldsymbol{x} \notin \Gamma$ and satisfy equation (1a) and condition (1b). In order to solve a given boundary value problem for ϕ, we need only find integral densities matching boundary conditions at Γ. This motivates a common technique in boundary integral methods [28], in which a potential function ϕ is written as a combination of these layer potentials. For example, consider the exterior Dirichlet boundary problem

$$\nabla^2 \phi(\boldsymbol{x}) - \lambda^2 \phi(\boldsymbol{x}) = 0 \ \ \forall \boldsymbol{x} \in \Omega_\infty, \qquad \phi = g \text{ on } \Gamma. \tag{6}$$

We propose the ansatz solution $\phi(\boldsymbol{x}) = (\mathcal{S}_\lambda + \mathcal{D}_\lambda)[\mu](\boldsymbol{x})$. Taking the limit as $x \to \Gamma$ in the normal direction, we then use well-known jump conditions for these potentials to obtain a boundary integral equation (BIE):

$$\frac{1}{2}\mu(\boldsymbol{x}) + (\mathcal{S}_\lambda + \mathcal{D}_\lambda)[\mu](\boldsymbol{x}) = g(\boldsymbol{x}) \quad \forall\, x \in \Gamma. \tag{7}$$

This is a Fredholm integral equation of the second kind; one can then establish via the spectra of these operators or using standard potential theory results that it is uniquely solvable [29]. This equation is generally well-conditioned, which is highly advantageous for its efficient numerical solution. A fast and accurate method for solving a discretized version of this equation is presented in Section 3.

Integral operators for Stokes problems

For the Stokes equations, the Stokeslet and Stresslet fundamental solutions are given by:

$$G(\boldsymbol{x}, \boldsymbol{y}) = \frac{1}{8\pi}\left(\frac{I}{\|\boldsymbol{x}-\boldsymbol{y}\|} + \frac{(\boldsymbol{x}-\boldsymbol{y})\otimes(\boldsymbol{x}-\boldsymbol{y})}{\|\boldsymbol{x}\|^3}\right), \tag{8a}$$

$$T(\boldsymbol{x}, \boldsymbol{y}) = -\frac{3}{4\pi}\left(\frac{(\boldsymbol{x}-\boldsymbol{y})\otimes(\boldsymbol{x}-\boldsymbol{y})\otimes(\boldsymbol{x}-\boldsymbol{y})}{\|\boldsymbol{x}-\boldsymbol{y}\|^5}\right). \tag{8b}$$

The Stokes single-layer potential, its associated traction kernel and the Stokes double-layer potential are given by

$$\begin{aligned}
\mathcal{S}[\sigma](\boldsymbol{x}) &= \int_\Gamma G(\boldsymbol{x}, \boldsymbol{y})\sigma(\boldsymbol{y})d\Gamma(\boldsymbol{y}),\\
\mathcal{K}[\sigma](\boldsymbol{x}) &= \int_\Gamma T(\boldsymbol{x}, \boldsymbol{y})\nu(\boldsymbol{x})\sigma(\boldsymbol{y})d\Gamma(\boldsymbol{y}),\\
\mathcal{D}[\sigma](\boldsymbol{x}) &= \int_\Gamma T(\boldsymbol{x}, \boldsymbol{y})\nu(\boldsymbol{y})\sigma(\boldsymbol{y})d\Gamma(\boldsymbol{y}).
\end{aligned} \tag{9}$$

A number of integral representations have been introduced for rigid body Stokes problems. In this context, we favor representations leading to well-conditioned integral equations (Fredholm of the 2nd kind) and prefer to avoid the introduction of additional unknowns or constraints. We employ the formulation in [25] for the Stokes mobility problem, which addresses both issues by representing the flow as the sum of two distinct single-layer potentials enforcing force and torque balance, and rigid body motion at particle boundaries, respectively. In Section 6, we describe a formulation based on a standard double-layer representation [30] to prescribe a tangential slip velocity at particle boundaries.

2.3 Spherical harmonic analysis

Working with the BIOs for screened Laplace and Stokes in Section 2.2 requires us to evaluate *weakly singular* and *hyper singular* integrals for targets $x \in \Gamma$. These operators are smooth when evaluated away from the surface, but they become *near-singular* as a target point x approaches Γ. Smooth numerical integration techniques

will degrade in quality unless discretization is greatly refined. In [24], analysis of integro-differential operators in spherical harmonic bases presented in [31, 32] was extended to all the Stokes BIOs, and applied to obtain an efficient, spectrally accurate evaluation scheme for both singular and near-singular cases. We present analysis of BIO signatures and derive evaluation formulas in solid harmonics for the screened Laplace operator. This allows us to extend this fast algorithm framework to the simulation of Janus particles in Section 3.

Spherical harmonics

The *spherical harmonic* of degree n and order m, denoted by Y_n^m, is given by

$$Y_n^m(\theta,\phi) = \sqrt{\frac{2n+1}{4\pi}}\sqrt{\frac{(n-|m|)!}{(n+|m|)!}}P_n^{|m|}(cos\theta)e^{im\phi}, \tag{10}$$

where P_n^m is the associated Legendre polynomial. The spherical harmonics are eigenfunctions of the screened Laplace equation on the unit sphere, forming an orthonormal basis for $L^2(S^2)$. It follows from a separation of variables argument that any solution to these equations on the interior or exterior of the unit sphere may be written as an expansion of solid harmonics

$$\phi_n^m(r,\theta,\phi) = f_n(r)Y_n^m(\theta,\phi), \tag{11a}$$

with

$$\phi(r,\theta,\phi) = \sum_{n=0}^{\infty}\sum_{m=-n}^{n}\alpha_n^m\phi_n^m(r,\theta,\phi). \tag{11b}$$

Layer potential spectra and evaluation formulas

Using the fact that solutions to the screened Laplace equation can be expanded as a superposition of solid harmonics ϕ_n^m, it can be shown that the spherical harmonics are eigenvectors of $\mathcal{S}_\lambda$ and $\mathcal{D}_\lambda$ on the sphere. We present here the eigenvalues for the modified Laplace equation. See Appendix A for a derivation using an argument analogous to that presented in [32].

Lemma 1 *(Screened Laplace operator spectra). On the unit sphere, the screened Laplace single- and double-layer operators diagonalize in the spherical harmonics basis Y_n^m and their spectra are given by*

	$\mathcal{S}_\lambda$	$\mathcal{D}_\lambda^+$	$\mathcal{D}_\lambda^-$
Y_n^m	$\frac{2\lambda k_n(\lambda)i_n(\lambda)}{\pi}$	$\frac{2\lambda^2 i_n'(\lambda)k_n(\lambda)}{\pi}$	$\frac{2\lambda^2 k_n'(\lambda)i_n(\lambda)}{\pi}$

with (i_n, k_n) the modified spherical Bessel functions of first and second kind, respectively. We use Lemma 1 to evaluate the single- and double-layer potentials off the surface of the spheres, arriving at the following results.

Theorem 1 *(Screened Laplace operator evaluation). The single- and double-layer potentials for density Y_n^m at an arbitrary point off the sphere with spherical coordinates (r, θ, ϕ) are:*

	$\mathcal{S}_\lambda[Y_n^m](r,\theta,\phi)$	$\mathcal{D}_\lambda[Y_n^m](r,\theta,\phi)$
$r > 1$	$\frac{2\lambda i_n(\lambda)}{\pi} k_n(\lambda r) Y_n^m(\theta,\phi)$	$\frac{2\lambda^2 i_n'(\lambda)}{\pi} k_n(\lambda r) Y_n^m(\theta,\phi)$
$r < 1$	$\frac{2\lambda k_n(\lambda)}{\pi} i_n(\lambda r) Y_n^m(\theta,\phi)$	$\frac{2\lambda^2 k_n'(\lambda)}{\pi} i_n(\lambda r) Y_n^m(\theta,\phi)$

Given a set of spherical harmonics coefficients μ_n^m for a given density μ, Theorem 1 allows us to evaluate layer potentials on and off the surface. It can be verified that the spectra of $\mathcal{S}'_\lambda$ and $\mathcal{D}'_\lambda$ are the derivatives of the above equations with respect to r. Formulas are given in Appendix B. The equations of Theorem 1 can easily be modified for potentials defined on spheres of different radii. See Appendix C for details.

3 Discretization

As described in the previous section, we rely on representations for ϕ and $\boldsymbol{u}$ as a combination of boundary integral operators. Following the work contributed for Stokes boundary integral operators in [24], we present a spectrally accurate evaluation scheme for the screened Laplace operators. Our goal is to develop a method of applying discretized operators $\mathcal{S}_\lambda$ and $\mathcal{D}_\lambda$ efficiently, so that equations like (7) may be efficiently solved by a Krylov subspace iterative method such as GMRES.

3.1 Janus interaction potential evaluation

Any numerical scheme for the approximate solution of BIEs in equation (7) will require accurate evaluation of integrals of the form

$$\boldsymbol{F_i}(\boldsymbol{x}) = \int_{\Gamma_i} K_i(\boldsymbol{x}, \boldsymbol{y}) \sigma_i(\boldsymbol{y}) dS(\boldsymbol{y}) \tag{12}$$

for points on and off the surface Γ_i. The operator of interest will then be the sum over all particles $\boldsymbol{F}(\boldsymbol{x}) = \sum_{i=1}^{M} \boldsymbol{F_i}(\boldsymbol{x})$. The integral kernel K_i contains a singularity when $x \in \Gamma_i$. To accurately compute $\boldsymbol{F}(\boldsymbol{x})$, we must be able to evaluate $\boldsymbol{F_i}$ in three regimes: when target points x are far from Γ_i (*smooth*), when they are on Γ_i (*singular*) and when they are close to Γ_i (*near-singular*).

We split the evaluation of integral densities at each particle into so-called *near* and *far* fields of targets. For targets in the far field, we employ a standard spectrally convergent smooth quadrature; for large numbers of particles, this computation is accelerated using the Fast Multipole Method (FMM). In the near field, we use the expansions in Theorem 1 to evaluate the BIOs of interest.

Smooth integration

Given a spherical harmonic order p, we sample at points $y_{j,k} = y(\theta_j, \phi_k)$ on each sphere with

$$\{\theta_j = \cos^{-1}(t_j)\}_{j=0}^{p}, \quad \left\{\phi_k = \frac{2\pi}{2p+2}\right\}_{k=0}^{2p+1}, \tag{13}$$

with t_j the $(p+1)$ Gauss-Legendre nodes in $[-1, 1]$ [33], for a total of $O(p^2)$ discretization points $y_{j,k}$ per particle, and $N = O(Mp^2)$ overall degrees of freedom. To illustrate, let us consider the single-layer potential from a single source sphere with surface Γ and radius r. We have

$$\mathcal{S}[\mu](\boldsymbol{x}) = \int_0^{2\pi}\int_0^{\pi} G(\boldsymbol{x}, \boldsymbol{y}(\theta,\phi))\mu(\theta,\phi)r^2 \sin\theta d\theta d\phi \tag{14}$$

for a target point x. If the integrand is smooth, this rule will be spectrally convergent as p increases. Although this is the case for any integrand with $x \notin \Gamma$, as x approaches the surface, our ability to represent this function and integrate it accurately with order p spherical harmonics degrades. Thus, we only employ this quadrature for targets that are *well-separated* from Γ, that is, such that

$$\text{dist}(\boldsymbol{x}, \Gamma) \geq \eta \text{diam}(\Gamma) = 2\eta r,$$

where η is determined by a user-defined target accuracy. We will refer to the set of well-separated points from Γ as its *far field*, and the complementary set as its *near field*.

The cost for directly evaluating all far-field interactions between M particles is (p^4M^2). Since this operation is a summation of Green's functions, Fast Multipole Method (FMM) [34] acceleration can be employed to reduce the cost to $O(p^2M)$. The FMM was originally developed for computations involving the Laplace kernel; it has since been extended to many PDEs of interest, including several implementations of the FMM for the screened Laplace kernel [35], as well as for the Stokes kernels [36]. We are currently employing the StokesLib3D package [37] for Stokes interactions and the FMMLIB3D package for Laplace interactions [38].

Singular integration

Gauss-Legendre quadrature will fail entirely when target points belong to the source sphere Γ_i. Such computations are required when calculating particle *self-interactions*. Singular integration on particles of spherical topology may be handled as in [33], using fast spherical grid rotations and FFT acceleration techniques. For spherical particles, the fact that BIOs of interest diagonalize in the spherical harmonics basis allows us to sidestep discretization of singular and hypersingular integrals.

To achieve this, we turn to the spectra of the single- and double-layer operators, described in Section 2.3. Suppose we have a function μ defined on the unit sphere and we wish to compute $\mathcal{S}_\lambda[\mu]$. We compute the spectra $\{\widehat{\mu}_n^m\}$ with a fast-forward

spherical harmonic transform (SHT). Truncating the spherical harmonic expansion at order p, we obtain the approximate equation

$$\mathcal{S}_\lambda[\mu](\theta,\phi) \approx \sum_{n=0}^{p}\sum_{m=0}^{n} \alpha_n^m \widehat{\mu}_n^m Y_n^m(\theta,\phi), \tag{15}$$

where eigenvalues α_n^m are given by Theorem 1. We evaluate these at all points of the spherical grid via an inverse SHT; FFT-accelerated SHT transforms are applied in $O(p^3 \log p)$ operations [39]. Fast $O(p^2 \log^2 p)$ SHTs are available; however, break-even points are typically large.

Near-singular integration

Finally, we must address the evaluation of a potential such as $\phi = \mathcal{S}_\lambda[\mu]$ at a nearby target point $\boldsymbol{x}$ off the unit sphere with spherical coordinates (r,θ,ϕ). Evaluation formulas in (1) allow us to represent points off the surface of a sphere in terms of spherical harmonics, yielding an expression of the form

$$\phi(\boldsymbol{x}) \simeq \sum_{n=0}^{p}\sum_{m=0}^{n} \alpha_n^m \kappa_n^m(r) Y_n^m(\theta,\phi), \tag{16}$$

where the vector of coefficients $\boldsymbol{\kappa}$ may be written as $\boldsymbol{\kappa}(r) = \mathcal{F}_\lambda(r)\widehat{\boldsymbol{\mu}}$. The operator $\mathcal{F}_\lambda$ is diagonal with entries dependent only on r.

The associated flux $\frac{\partial\phi}{\partial v_x}$ (the normal derivative of ϕ) may be evaluated using this same scheme. However, the linear operator mapping $\widehat{\boldsymbol{\mu}}$ to the spherical harmonic coefficients for $\frac{\partial\phi}{\partial v_x} = \mathcal{S}_\lambda[\boldsymbol{\mu}]$ will be tridiagonal, and its entries will depend on θ and ϕ as well as r. The derivation of this result is identical to that for the Laplace equation, as discussed in [24]. Since v_x depends on target x, it may have normal and tangential components relative to source sphere Γ. The derivative of each term in (16) is

$$\frac{\kappa(r)Y_n^m(\theta,\phi)}{\partial v_x} = \kappa'(r)(v_x^T \boldsymbol{e}_r)Y_n^m(\theta,\phi) + \kappa(r)\left(v_x^T \nabla_\Gamma Y_n^m(\theta,\phi)\right) \tag{17}$$

where ∇_Γ is the surface gradient. $\nabla_\Gamma Y_n^m$ may be written as a combination of Y_n^m, Y_{n-1}^m, Y_{n+1}^m. The tridiagonal map mentioned above can be obtained by applying (17) to an expansion in solid harmonics like (16).

We use this scheme to evaluate interactions between a particle and target points intersecting its near field. Parameters η and p must be chosen carefully to balance accuracy and cost of near and far evaluation routines. Since the number of particles neighboring a fixed particle is bounded, the maximum number of near-field target points per particle is $O(p^2)$. Direct evaluation of (16) is thus $O(p^4)$ per particle. Efficient $O(p^3 \log p)$ accelerations based on FFTs or translation operators are proposed in [24].

3.2 Computation of scalar influence on fluid flow

To evaluate the coupling between Janus interactions and the fluid, we need to compute $\nabla\phi$. We decompose the gradient as

$$\nabla\phi = \nabla_\Gamma\phi + \frac{\phi}{\partial v}\boldsymbol{n}, \tag{18}$$

where ∇_Γ is the surface gradient. $\nabla_\Gamma\phi$ can be expressed in terms of angular derivatives of the first fundamental forms of the surface. For spherical bodies, these values may be computed explicitly. Since particle shapes do not change, the surface gradient operator is fixed and may be precomputed as a matrix. To compute the normal derivative, we again employ properties of the single- and double-layer operators. For instance, for the ansatz proposed in Section 2.2, we have that

$$\frac{\partial\phi}{\partial v_x} = (\mathcal{S}'_\lambda + \mathcal{D}'_\lambda)[\mu] \tag{19}$$

for a target point outside the particle. For points on the surface, we use the appropriate jump conditions. For instance, as $x \to \Gamma$ from the outside,

$$\frac{\partial\phi}{\partial v_x} = (\mathcal{S}'_\lambda + \mathcal{D}'_\lambda)[\mu] - \frac{1}{2}\mu \tag{20}$$

These quantities are computed using the same technique described in Section 2.3, with the operator spectra given in Appendix B. $\nabla\phi$ may thus be computed at the cost of multiplication by a precomputed matrix and one additional layer potential evaluation.

3.3 Particle evolution and collision resolution

As was outlined in Section 2, the Janus interaction potential ϕ is formulated as a combination of layer potentials; given a configuration of M rigid Janus particles, the evaluation routines in Section 3.1 allow us to efficiently solve the corresponding BIE via a Krylov subspace method. Given the resulting net forces and torques in (3), we then employ techniques in [24] to solve the relevant Stokes rigid body problem and find translational and rotational velocities. Finally, standard explicit time discretization schemes are used to evolve rigid particle positions and rotation frames in time. This sequence is repeated each timestep; the resulting particle evolution algorithm is illustrated in Fig. 1.

When particles are in close proximity to each other or to the geometry, potential collisions must be detected and resolved. This must be done carefully to preserve both cost-efficiency and physical fidelity. Following the approach in [23], we employ a linear complementary formulation (LCP) of contact; for each colliding pair of particles, a normal force must be applied to prevent interpenetration. In this work, we employ the state-of-the-art Barzilai-Borwein Projected Gradient Descent method (BBPGD) to find the unknown contact forces, adding them to Janus interaction forces and torques

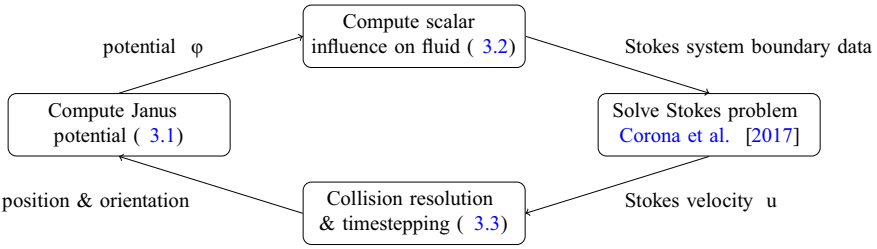

Fig. 1 Advancing the system by a single time step requires us to: (i) solve the Janus interaction potential BIE, (ii) setup and solve the corresponding Stokes rigid body problem, (iii) use the Stokes formulation to resolve collisions via the LCP, and (iv) given rigid body velocities, advance particle positions and orientations

for particle evolution [40]. We note that each iteration of the PGD involves solving a Stokes rigid body problem; in our experiments, the number of iterations remains small ($\lesssim$ 10 PGD iterations).

3.4 Validation

We construct a simple boundary value problem to test the accuracy of our near evaluation routine. For a system of 3 spheres of different radii, we consider the potential induced by point charges randomly placed inside each sphere; this potential can be easily evaluated at targets x as a weighted sum of Green's functions $G(\boldsymbol{x}, \boldsymbol{x_i})$ for each point charge $\boldsymbol{x_i}$. To test our evaluation scheme, we evaluate the potential induced on each surface, solve the Dirichlet BIE in (7), and use the integral representation to evaluate it at shells of target points at distance $(10^{-k})r_i$ from each spherical surface. The results in Fig. 2 demonstrate spectral accuracy independent of the distance between the surface and target.

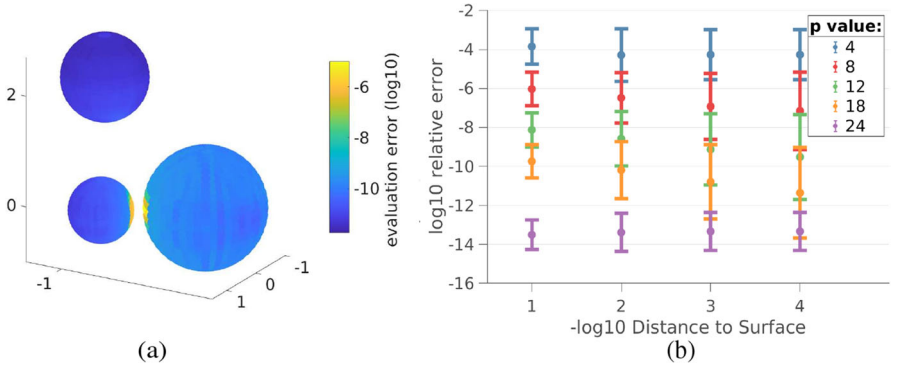

Fig. 2 Evaluation test consisting of three spheres with centers (-1.5,1,0),(-3,0,0),(-1,0 2) and radii 0.5,1,0.7, respectively (a). We evaluate the potential at spherical target shells located at distance $(10^{-k})r_i$ from each surface, for $k = 1, ..., 4$. We plot the relative error distribution, and observe that it does not increase as target points approach particle surfaces, and it decays spectrally as p increases (b)

4 Amphiphilic particles

Amphiphilic particles are split into a hydrophilic head and hydrophobic tail. Suspensions of such particles serve as mimetic models for cell membrane dynamics and are widely used in self-assembling nanomaterials. We first describe an integral formulation for amphiphilic Janus interactions. We then use our simulation framework to demonstrate spontaneous self-assembly of micelles in three-dimensional systems.

4.1 Formulation

We employ the model developed by Fu et al. [7], which formulates hydrophobic interaction potentials in integral form. The hydrophobic interaction potential ϕ is defined as the smooth minimizer of the hydrophobic energy functional for a given particle configuration and Dirichlet boundary value f:

$$E[\phi] = \int_{\Omega_\infty} \|\nabla\phi\|^2 + \frac{1}{\rho^2}\phi^2 dV = \int_\Gamma \phi \frac{\partial\phi}{\partial\nu} d\Gamma. \tag{21}$$

The equality of the two integrals follows from Green's identities and equation (22) below. E is derived from a quadratic expansion of the film tension on a sphere, the details of which are given in sources such as [41, 42]; it is used to investigate lipid membrane interactions in [43]. Through variational methods, E can be shown to have a unique minimum which satisfies the screened Laplace equation

$$-\rho^2\nabla^2\phi(\boldsymbol{x}) + \phi(\boldsymbol{x}) = 0 \quad \boldsymbol{x} \in \Omega_\infty, \quad \phi(\boldsymbol{x}) = f \quad \boldsymbol{x} \in \Gamma, \tag{22}$$

where f describes the hydrophobic character of the boundary with $0 < f < 1$ and ρ is a characteristic length of attraction. We recover the screened Laplace equation in standard form by setting $\lambda = \frac{1}{\rho}$. In our simulations we take f to be a shifted cosine function, $f(\theta) = \frac{1}{2}(\cos\theta + 1)$, where θ is the co-latitude of a point on the particle surface. Figure 3 shows a cross section of the resulting potential for two values of λ.

Integral equation formulation

As the hydrophobic potential ϕ satisfies the screened Laplace equation, we make use of the ansatz proposed in equation (7); the exterior Dirichlet problem in equation (22) leads to the BIE

$$f(\boldsymbol{x}) = \frac{1}{2}\mu(\boldsymbol{x}) + (\mathcal{S}_\lambda + \mathcal{D}_\lambda)[\mu](\boldsymbol{x}) \quad \boldsymbol{x} \in \Gamma. \tag{23}$$

The corresponding stress tensor [7] can be shown to be

$$\mathcal{T}_J = \eta\left(\frac{\phi^2}{\rho^2}I + 2\left(\frac{1}{2}\|\nabla\phi\|^2 - \nabla\phi\otimes\nabla\phi\right)\right). \tag{24}$$

In this expression, all of the units are nondimensionalized and η is the ratio of the amphiphilic to viscous pressure, $\eta = \pi_a/\pi_v$. Expressions for these pressures are presented in Appendix D.

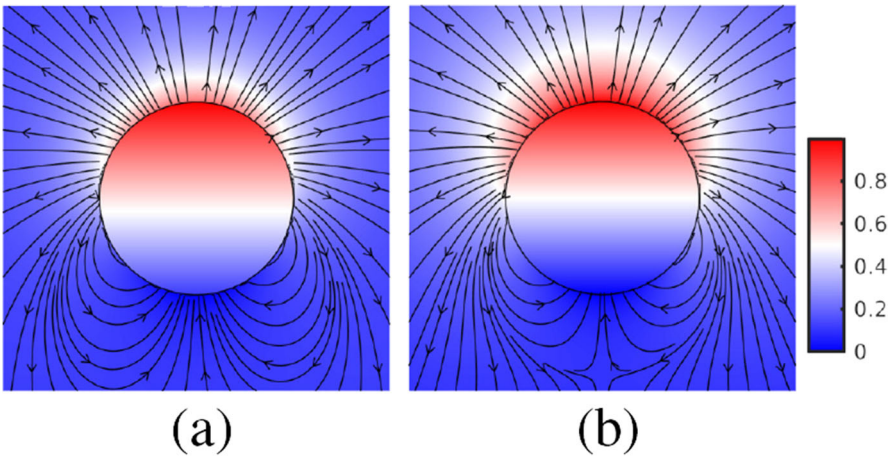

Fig. 3 Amphiphilic potential of a particle with $\lambda = 1$ (a) and 0.1 (b) with field lines drawn. The comparison between these figures illustrates the effect of λ on the potential decay due to the conductive properties of the fluid medium

4.2 Self-assembly

Employing our boundary integral approach, we simulate self-assembly in systems of amphiphilic particles. In all of these examples we use the average particle radius, r, as the characteristic unit length. If we let the particle radius be $1nm$, with $\gamma = 1\frac{pN}{nm}$ and $\mu = 1cPas$ then the time unit is $10^{-8}s$, where nondimensionalized time is given by the expression $t = \frac{r\mu}{\gamma}$. We have chosen $\Delta t = 0.1$ in these simulations, so that one timestep corresponds to 1×10^{-9} seconds. Likewise, we report nondimensionalized energy so that one unit corresponds to γ times unit length squared. In the following examples this corresponds to 10^{-21} joules. These parameter values are used in the following experiments, except where otherwise stated.

Four particle system

To illustrate this phenomenon, we first present a small example involving four amphiphilic spheres of the same size; these are initialized with random initial positions and orientations. In such a situation, the particles are known to form a tetrahedral configuration. Figure 4 shows the initial and final configurations of the spheres as well as cross-sectional plots of the resulting potential, agreeing with two-dimensional results in [7, 44]. The particles seek to minimize contact between the fluid and the hydrophobic tails by shielding them in the center of the configuration.

Micelle formation

We then explore the dynamics of larger systems of amphiphilic particles. In [7] the authors studied the long-term configurations resulting from two-dimensional amphiphilic interactions. We recreate their experiment here in three dimensions. Figure 5 shows the final configurations for two instances of the corresponding three-dimensional experiment; in both, a single-layer structure (micelle) forms as particles cluster with their hydrophobic ends facing inwards.

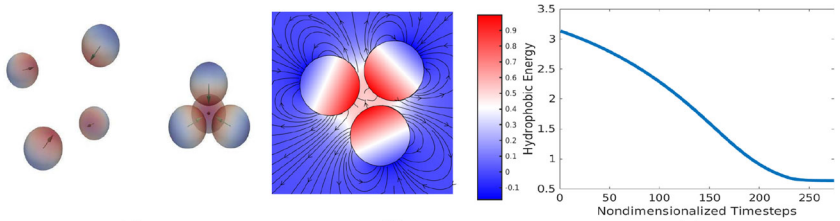

Fig. 4 Systems of four amphiphilic particles form a tetrahedral configuration (a). We plot the hydrophobic potential on a cross section through a base of the tetrahedron (b), illustrating the higher potential region between particles. Finally, we plot the hydrophobic energy as the tetrahedron forms (c)

We observe micelles to be the most common long-term configurations; their formation does not appear to depend strongly on initial conditions or the number of particles. However, the resulting micelles are more tightly packed for certain numbers of particles. We observe the formation of other stable structures, such as bilayer sheets, when the initial configuration is sufficiently close to the final configuration. In two-dimensional experiments, bilayers are observed to form spontaneously [7]. We do not notice such spontaneity across our experiments in three dimensions.

5 Bipolar electric particles

We present a model for bipolar electric Janus particles. These particles display concentrations of charge density of opposite signs on their northern and southern hemispheres. Such particles have been shown to exhibit self-assembly behavior such as the formation of chains [45], and can be manipulated through careful application of electric and magnetic fields [46, 47].

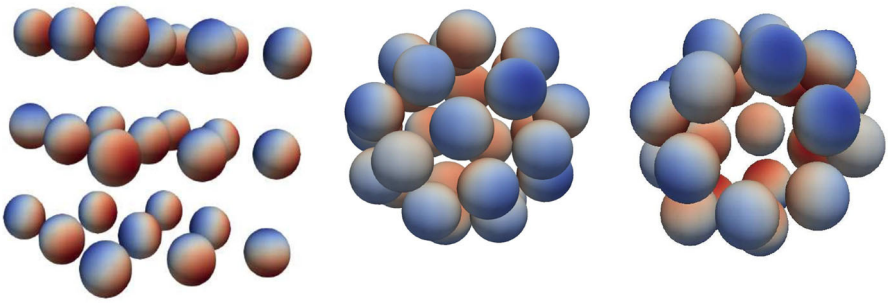

Fig. 5 Three-dimensional configurations of particles tend to form micelles, with their hydrophobic ends pointing inwards. We demonstrate with a $3 \times 3 \times 3$ lattice of particles with random initial orientation (a) and the resulting structure (b). When three particles are removed from the configuration, the resulting configuration is less tightly packed (c)

5.1 Formulation

We assume particle interiors are perfect conductors and their interactions are electrostatic. We wish to follow the model employed in [48] in which a constant electric field E_0 is applied. However, if the fluid is an imperfect conductor ($\lambda > 0$), a constant electric field is not physical. To resolve this, we confine our experiments to the interior of a rigid spherical shell, $\Omega_{sh} = \Omega \cup \Omega_\infty$ with boundary Γ_∞, allowing a constant field applied to the shell boundary to permeate into the fluid. In this setting, Maxwell's equations reduce to coupled Laplace (particle interiors) and screened Laplace (exterior) equations for ϕ, the scalar electrostatic potential. Particle interiors are assumed to have uniform electric permittivity, ϵ_i, while the exterior has permittivity ϵ_0. We normalize the permittivity by dividing through by ϵ_0, so that the exterior permittivity is 1 and the interior permittivity is $\epsilon = \epsilon_i/\epsilon_0$.

Mathematical model

Gauss's Law states that for a charge distribution ρ, the resulting electrostatic force potential ϕ must satisfy

$$\nabla \cdot (\epsilon \nabla \phi) = \rho. \tag{25}$$

In the particle interior, Gauss's law simplifies to a Poisson equation. The charge distribution, ρ, is prescribed at the start. We choose ρ to be the charge induced by a pair of point charges of equal strength and opposite sign in the interior of the particle. In the exterior, we model the electrostatic potential described by the linearized Poisson-Boltzmann equation, the derivation of which can be found in [49]. We arrive at the following system of equations with boundary conditions:

$$\nabla^2 \phi = \frac{1}{\epsilon}\rho, \quad \boldsymbol{x} \in \Omega, \qquad \nabla^2 \phi - \phi = 0, \quad \boldsymbol{x} \in \Omega_\infty \tag{26}$$

$$[[\phi]]_\Gamma = 0 \qquad \left[\left[\epsilon(\boldsymbol{x})\frac{\partial \phi}{\partial v}\right]\right]_\Gamma = 0. \tag{27}$$

All physical quantities have been nondimensionalized in the manner described in Appendix D.

Boundary integral formulation

We derive a novel boundary integral equation formulation for the electrostatic potential ϕ. A similar direct second-kind formulation based on Green's theorems was derived and analyzed in [50, 51]. This system has mixed boundary conditions and requires the evaluation of interior potentials. We represent the potential with a pair of unknown densities, ψ and μ. The potential induced from point charges in the interior is denoted by $\mathcal{Q}$. The potential from the exterior field, $\mathcal{E}$, is represented as a constant electric field in the exterior of the shell and as a layer potential in the shell interior:

$$\mathcal{E}(\boldsymbol{x}) = \boldsymbol{E}_0^T \boldsymbol{x} \quad \boldsymbol{x} \in \Gamma_\infty, \tag{28}$$

$$\mathcal{E}(\boldsymbol{x}) = (\mathcal{S}_\lambda + \mathcal{D}_\lambda)[\mu_\infty](\boldsymbol{x}) \quad \boldsymbol{x} \in \Omega_\infty. \tag{29}$$

μ_∞ is determined by equating the two expressions at the boundary and solving the resulting integral equation at the beginning of our simulation. We then make the following ansatz, expressing ϕ as

$$\begin{aligned}\phi(\boldsymbol{x}) &= \mathcal{S}_0[\psi](\boldsymbol{x}) + \mathcal{D}_0[\mu](\boldsymbol{x}) + Q(\boldsymbol{x}) \quad \boldsymbol{x} \in \Omega, \\ \phi(\boldsymbol{x}) &= \mathcal{S}_\lambda[\psi](\boldsymbol{x}) + \mathcal{D}_\lambda[\mu](\boldsymbol{x}) + \mathcal{E}(\boldsymbol{x}) \quad \boldsymbol{x} \in \Omega_\infty.\end{aligned} \tag{30}$$

This formulation automatically satisfies the Poisson and Poisson-Boltzmann equations on the respective domains. Enforcing the jump conditions, we obtain the following system of equations for $\boldsymbol{x} \in \Gamma$:

$$\begin{aligned}0 &= (\mathcal{S}_\lambda - \mathcal{S}_0)[\psi](\boldsymbol{x}) + (\mathcal{D}_\lambda - \mathcal{D}_0)[\mu](\boldsymbol{x}) + \mu(\boldsymbol{x}) - (\mathcal{E} - Q)(\boldsymbol{x}), \\ 0 &= (\mathcal{S}'_\lambda - \mathcal{S}'_0)[\psi](\boldsymbol{x}) + (\mathcal{D}'_\lambda - \mathcal{D}'_0)[\mu](\boldsymbol{x}) - \psi(\boldsymbol{x})/2 - \epsilon\psi(\boldsymbol{x})/2 \\ &\quad - \left(\frac{\partial \mathcal{E}}{\partial v} - \epsilon\left(\frac{\partial Q}{\partial v}\right)\right)(\boldsymbol{x}).\end{aligned} \tag{31}$$

We may then set the following matrix equation by evaluating Q and $\frac{\partial Q}{\partial v}$ on the boundary

$$\begin{pmatrix} I + \mathcal{D}_\lambda - \mathcal{D}_0, & \mathcal{S}_\lambda - \mathcal{S}_0 \\ \mathcal{D}'_\lambda - \epsilon\mathcal{D}'_0 & -\frac{(1+\epsilon)}{2} I + \mathcal{S}'_\lambda - \epsilon\mathcal{S}'_0 \end{pmatrix} \begin{bmatrix} \mu \\ \psi \end{bmatrix} = \begin{pmatrix} \mathcal{E} - Q \\ \epsilon\left(\frac{\partial \mathcal{E}}{\partial v} - \frac{\partial Q}{\partial v}\right) \end{pmatrix}. \tag{32}$$

This is a coupled, second-kind system of BIEs for densities μ, ψ. Once solved, we use expressions in equations (30) to find the potential ϕ at arbitrary points. We use the Maxwell stress tensor to compute forces and torques. Rigid particle translational and rotational velocities are then computed by solving the Stokes mobility problem.

5.2 Numerical experiments

In Fig. 9 we reproduce as closely as possible a two-dimensional experiment presented in [48]. Bipolar particles are initially placed in a diagonal arrangement. In this setup the time nondimensionalization is given by $t = \frac{q_c^2 \mu}{\epsilon_0 \|\boldsymbol{E_0}\|^2}$. In our experiments we use cC as the base unit of charge and $0.01 V/\mu m$ as the units of field strength, as well as taking the viscosity μ to be $1\, mPas$. We take the unit length to the radius of a particle, which we set to be $1\mu m$. The radius of the confined system, r_{sh} is set to 25 units. The charge orientation of each particle is initially aligned with the x axis, perpendicular to the external field, which points in the direction of the negative y axis. In terms of our nondimensionalized units, we have $q_c = 50$ and $\|\boldsymbol{E_0}\| = 10$.

The electric force imbalance on the particles induces clockwise rotation of both the particles and the line, as the particles form a chain in the direction of the induced electric field. Figure 6 shows the streamlines from the flow field that result from particle interaction. Initially, rapid local rotations are present in the fluid as the particles rotate. After this occurs, the flow becomes more globally rotational, and the particles form a chain aligned in this direction.

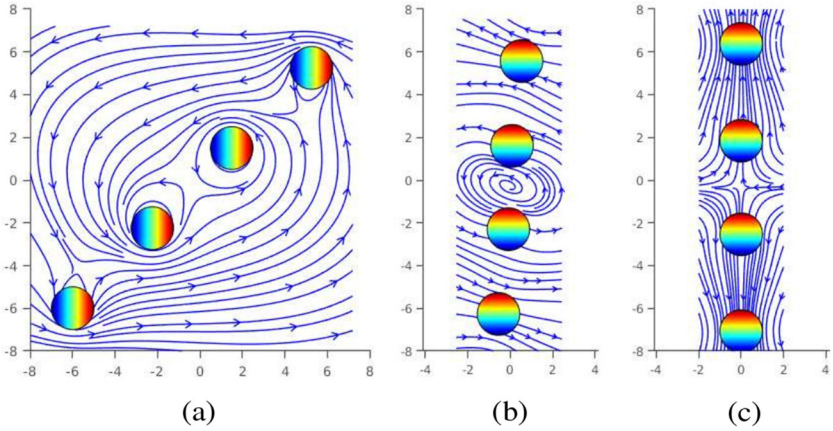

Fig. 6 We simulate an experiment described in [48], where bipolar electric particles were placed in the configuration (a). Particles are colored according to surface charge; red and blue represent positive and negative, respectively. A constant electric field is applied in the positive y direction, causing the particles to rotate in the direction of the field (b), while the entire line moves to align with the field (c). Fluid streamlines illustrate the initial rapid rotation of the individual particles and slower rotation of the chain. The maximum fluid speed of the second and third panels are, 3%, and 0.5% of the maximum initial speed, respectively

We then conducted larger-scale experiments to study spontaneous chain formation in three dimensions; snapshots of one such experiment are shown in Fig. 7. We place 125 particles with random orientations and with initial positions on a lattice offset from the direction of the electric field. Initially, a locally rotational flow forms as particles rotate to align with the electric field, whereupon chain formation is observed. As chains form, they also begin to repel each other. Throughout this simulation, we quantify the extent of polarization by plotting the distribution of particle angles relative to the background field, as is shown also in Fig. 7d.

Across all our three-dimensional experiments, we observe spontaneous chain formation irrespective of initial positions or orientations, closely matching previous results in two-dimensional studies. This confirms that, by changing the external field, one can effectively control the orientation of the particles and induce chain formation.

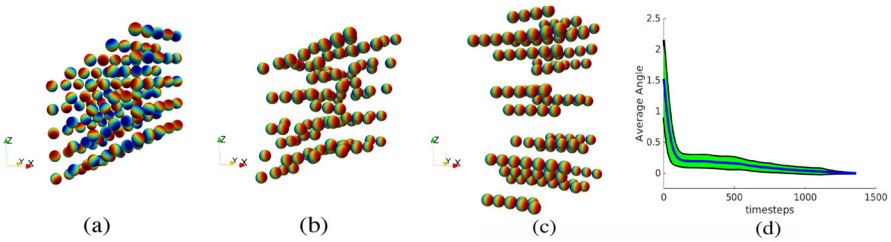

Fig. 7 125 bipolar particles are oriented randomly (a). When an external electric field is applied in the direction of the x axis, the particles orient themselves in that direction (b) and form chains (c). To quantify polarization, we plot the distribution of angles that the particles make with the electric field (d)

6 Phoretic particles

Phoretic particles are a class of Janus particles with interactions driven by fluid slip on their surface; in this work, we discuss a type of phoretic particle driven by chemical reactions with a solute. Phoretic particle suspensions are useful for modeling microswimmers, particles that propel themselves by "pushing" or "pulling" the surrounding fluid. Spherical phoretic particles are also of great interest as drug delivery mechanisms in biological systems.

We employ a standard mathematical formulation for phoretic particles, described in [9]. This formulation models phoretic particle interactions via diffusion of chemical concentrations in solution inducing a tangential slip velocity on particle surfaces. As the main coupling between Janus and hydrodynamic interactions is due to this tangential slip, the resulting rigid body problem is not a mobility problem; we detail an integral formulation for the resulting Stokes problem.

6.1 Formulation

In the model we employ, the phoretic character of a particle is determined by two functions on the particle surface, $A(\theta)$ and $M(\theta)$. $A(\theta)$ governs the flux of chemical concentration at each particle surface, while $M(\theta)$ models how concentration gradients induce tangential slip on the fluid.

Consider M rigid spherical Janus particles suspended in a fluid with viscosity μ inside a closed domain Ω_∞. Let $\{\Omega_k, \Gamma_k\}_{k=1}^M$ denote the domains and boundaries of the rigid particles respectively. The chemical concentration C is determined by solving a Laplace Neumann boundary value problem:

$$\nabla^2 C = 0 \quad \text{in} \quad \Omega_\infty, \tag{33a}$$

$$\frac{dC}{dn} = A_\infty \quad \text{on} \quad \Gamma_\infty, \tag{33b}$$

$$\frac{dC}{dn} = -A_k(\theta_k) \quad \text{on} \quad \Gamma_k, \quad k = 1, \ldots, N. \tag{33c}$$

Solutions must satisfy the compatibility condition that $\int_{\Gamma_\infty} A_\infty = \sum_{k=1}^M \int_{\Gamma_k} A_k dS_k = 0$. In an unbounded context, the flux condition on the boundary is replaced with the far-field condition that $\lim_{\|x\|\to\infty} C(x) = 0$. The concentration gradient induces a tangential slip velocity, given by

$$\boldsymbol{u}^k_{slip} = M_k(\theta_k)(I - \boldsymbol{nn}^{\boldsymbol{T}})\nabla C \quad \text{on} \quad \Gamma_k. \tag{34}$$

The corresponding equations for the fluid velocity are given by:

$$-\nabla p + \nabla^2 \boldsymbol{u} = 0 \quad \text{in} \quad \Omega_\infty, \tag{35a}$$

$$\nabla \cdot \boldsymbol{u} = 0 \quad \text{in} \quad \Omega_\infty, \tag{35b}$$

$$\boldsymbol{u} = 0 \quad \text{on} \quad \Gamma_\infty, \tag{35c}$$

$$\boldsymbol{u} = \boldsymbol{u}^k_{slip} + \boldsymbol{v}^k + \boldsymbol{\omega}^k \times (\boldsymbol{x}^k - \boldsymbol{c}^k) \quad \text{on} \quad \Gamma_k, \quad k = 1, \ldots, N, \tag{35d}$$

$$\int_{\Gamma_k} \boldsymbol{f}\, d\Gamma_k = -\boldsymbol{F}_k \text{ and } \int_{\Gamma_k} (\boldsymbol{x^k} - \boldsymbol{c}^k) \times \boldsymbol{f}\, d\Gamma_k = -\boldsymbol{T}_k, \quad k = 1, \ldots, N. \tag{35e}$$

This system closely resembles the formulation of the Stokes mobility problem in equations (4). However, in this case, the Laplace potential is mainly coupled to the Stokes equation through an induced slip velocity, rather than through rigid body forces and torques, $\mathbf{F}_k$ and $\mathbf{T}_k$, which are both equal to zero unless particles are in contact with each other or the domain boundary Γ_∞. We present an integral representation tailored to this tangential slip problem below.

6.2 Boundary integral formulation

In this case, the scalar potential ϕ corresponding to Janus particle interactions must satisfy the Laplace Neumann BVP in (33c); we follow the standard approach for this problem representing it as a single-layer potential defined on $\Gamma \cup \Gamma_\infty$ [29]. The Stokes potential in this case is more involved. We outline the steps below.

Stokes integral formulation

We begin by making the ansatz that the fluid velocity $\boldsymbol{u}(\boldsymbol{x})$ can be expressed as

$$\boldsymbol{u}(\boldsymbol{x}) = \mathcal{D}_\infty[\boldsymbol{\mu}_\infty](\boldsymbol{x}) + \sum_{k=1}^{M} (\mathcal{D}_k + \mathcal{V}_k)[\boldsymbol{\mu_k}](\boldsymbol{x}), \tag{36}$$

where $\mathcal{V}_\infty[\mu_\infty]$ is a rank 1 correction for the Stokes double-layer interior operator given by

$$\mathcal{V}_\infty[\boldsymbol{\mu}](\boldsymbol{x}) = \frac{1}{4\pi} \boldsymbol{e_r}(\boldsymbol{x}) \int_{\Gamma_\infty} (\boldsymbol{\mu} \cdot \boldsymbol{e_r}) dS \tag{37a}$$

on the bounding surface and $\mathcal{V}_k[\mu_k]$ is the standard completion flow [30], with

$$\mathcal{V}_k[\boldsymbol{\mu}](\boldsymbol{x}) = G(\boldsymbol{x} - \boldsymbol{c_k}) \int_{\Gamma_k} \boldsymbol{\mu}(\boldsymbol{x}) dSy + R(\boldsymbol{x} - \boldsymbol{c_k}) \int_{\Gamma_k} (\boldsymbol{y} - \boldsymbol{c_k}) \times \boldsymbol{\mu}(\boldsymbol{y}) dS(\boldsymbol{y}) \tag{37b}$$

on the surface of each particle, where $G(r)$, $R(r)$ are the Stokeslet and Rotlet, respectively.

By substituting these expressions into equations (36) and taking the limit as x approaches each component of the boundary in the normal direction, we obtain a second-kind BIE. The force and torque balance boundary condition remain the same, with

$$\int_{\Gamma_k} \boldsymbol{\mu} dS_k = \boldsymbol{F_k}, \quad \int_{\Gamma_k} \boldsymbol{\mu} \times (\boldsymbol{x} - \boldsymbol{c^k}) dS_k = \boldsymbol{T}_k. \tag{38}$$

Overall, we have a system of BIEs for the Stokes equations of the form:

$$\begin{bmatrix} -\frac{1}{2}I + \mathcal{D}_\infty + \mathcal{V}_\infty & \sum_{k=1}^{M}(\mathcal{D}_{k,\infty} + \mathcal{V}_{k,\infty}) & 0 \\ \mathcal{D}_{\infty,k} & (\frac{1}{2}I + \sum_{k=1}^{M}(\mathcal{D}_k + \mathcal{V}_k)) & -G \\ 0 & H & 0 \end{bmatrix} \begin{bmatrix} \boldsymbol{\mu}_\infty \\ \boldsymbol{\mu}_{RB} \\ \boldsymbol{V}_{RB} \end{bmatrix} = \begin{bmatrix} 0 \\ \boldsymbol{U}_{slip} \\ \boldsymbol{F}_{RB} \end{bmatrix}. \quad (39)$$

Here, $\boldsymbol{U}_{slip}$ is a vector of the slip velocities on each particle, $\boldsymbol{V}_{RB}$ is a vector consisting of v and ω for each particle, and $\boldsymbol{F}_{RB}$ is a vector of corresponding rigid body forces and torques. G is a block-diagonal operator mapping $\boldsymbol{V}_{RB}$ to rigid body motion velocities at particle boundaries and H is a block-diagonal operator that computes the two integrals in (38).

The system of equations in (39) is then solved at every timestep with $\boldsymbol{F}_{RB}$ set to zero. If other forces are present, such as those from contact resolution, (39) is then solved a second time with nonzero $\boldsymbol{F}_{RB}$, using the first solution and complementarity to facilitate this second solve.

6.3 Results

A wide range of phoretic particles can be modeled by the functions A and M. For our studies, we will focus on simulating systems of so-called Saturn particles [52], which are defined by prescribing

$$A_k(\theta) = a_k(1 - \cos^2\theta), \quad M_k(\theta) = m_k \cos\theta. \quad (40)$$

A single such particle in free space has speed $\frac{4}{45}a_k m_k$ in the direction of the particle head. Even for p as low as four, we find that the velocity of a single particle in the simulations matches the theory with 15 digits of accuracy. We plot the flow generated from a single particle in Fig. 8, propelling the particle forward.

Pairwise interactions

We observe patterns of pairwise interactions when two particles are confined in a shell. In Fig. 8 we plot the trajectory of two particles in a symmetric orbit. We observe similar pairwise interaction behavior to that discussed in [9], which studied how inter-

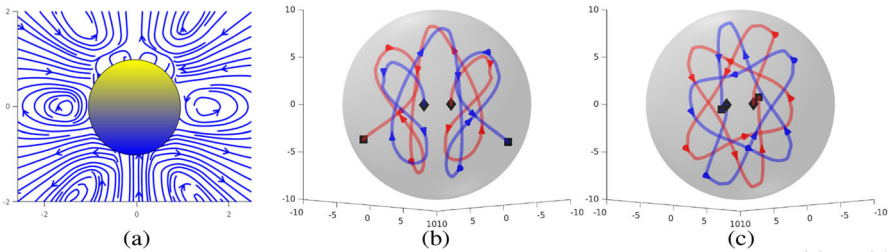

Fig. 8 We plot the fluid field of a single phoretic particle oriented in the positive y direction (a). In (b) and (c), two particles are placed in a shell of radius 10, with starting position denoted with a diamond. The particles are initially aligned in (b) and anti-aligned in (c). We plot the trajectories of the particle centers in the xz plane

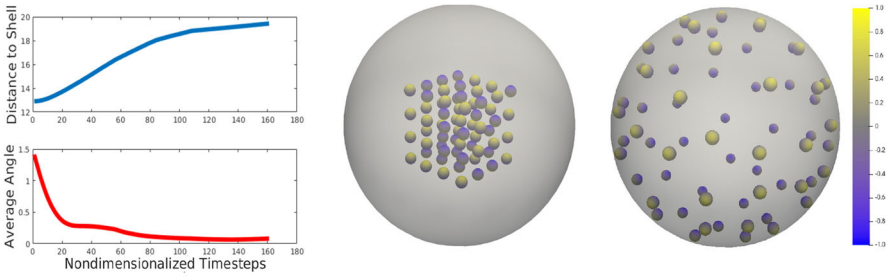

Fig. 9 We place a $4 \times 4 \times 4$ grid of phoretic particles in a confining shell of radius 25. (b) The particles spread out and migrate to the shell, orienting themselves in the direction of the shell normal (c). The plots in (a) show the average distance between the particles and the shell and the average alignment between the particles and the shell normal at the point of contact

actions between particle pairs depended on their relative orientations, observing that anti-aligned particles tend to orbit each other.

Many-body interactions

Understanding the behavior of many-body phoretic suspensions is considerably more challenging. Previous studies of these systems tend to make a number of generalizations, such as assuming A_k and M_k to be constant on each hemisphere, or assuming the domain to be quasi-two dimensional and semi-infinite, as in [9]. In our case, we set the confining geometry Ω_∞ to be a sphere. We set the flux on the boundary to be such that the total flux on the system is 0:

$$\frac{dC}{dv} = \frac{1}{4\pi R_\infty^2} \sum_{k=1}^{M} \int_{\Gamma_k} A_k(\theta_k). \tag{41}$$

With this configuration, we observe that the particles are attracted to the boundary of the shell, orienting themselves in the direction normal to the shell. This particle migration occurs rapidly (Fig. 9).

7 Conclusions

We presented a general computational framework for the simulation of dense Janus particle suspensions in Stokes flow. Our approach features integral representations of long-range Janus particle interactions; for this purpose, we have contributed efficient and spectrally accurate scalar potential evaluation methods for screened Laplace potentials. To resolve resulting fluid flow and particle collisions, we leverage recent developments in fast algorithms for high-fidelity Stokes rigid body problems.

All numerical solvers proposed for this framework are spectrally accurate, efficient and scalable with problem size. Due to the favorable conditioning of the BIEs involved and our use of efficient evaluation schemes for both near-field and far-field spherical particle interactions, computational cost scales linearly with the number of

particles. We note that, provided efficient singular and near-singular integral evaluation schemes are developed, it can be readily applied to wide classes of particle shapes and confining geometries. We are currently investigating the extent to which the spectral analysis techniques we have described can be extended to spheroidal, ellipsoidal and axisymmetric shapes.

Due to the nature of the physical fields involved in most relevant Janus particle types, the approach presented in this work has wide applicability. We demonstrate this through three distinct case studies of Janus particles of great relevance to applications in biomedicine and materials science: amphiphilic, bipolar electric, and phoretic particles. We note these examples do not constitute an exhaustive list; a number of additional Janus particle systems can be modeled by following the process outlined in this work. For instance, the bipolar formulation presented in this work may be readily adapted to problems in magnetic Janus particle suspension simulation [11, 47]. Moreover, the techniques presented here may be relevant to a larger class of active matter systems, for example, in the simulation of chemotactic bacterial suspensions.

In each of these studies, we show how to design integral representations for the Janus interaction potential, leading to well-conditioned second-kind boundary integral equations; depending on the coupling between Janus and hydrodynamic interactions, the corresponding integral equation-based Stokes rigid body solver is deployed. The ability to accurately simulate these suspensions allows us to recreate spontaneous self-assembly for moderately large systems of particles in a single processor; our experience with hybrid HPC implementations such as [23] suggests the methods proposed here could be readily scaled to enable large-scale simulations on distributed-memory machines.

Acknowledgements We acknowledge the Mcubed program at the University of Michigan (UM). The authors also acknowledge the computational resources and services provided by UM's Advanced Research Computing.

Funding This work received support from NSF under grants DMS-1719834, DMS-1454010 and DMS-2012424

Declarations

Conflict of interest The authors declare no competing interests.

Appendix A. Derivation of the layer spectra

In Theorem 1, formulas for the spectra of $\mathcal{S}$ and $\mathcal{D}$ were presented. We outline the derivation of these values below, following [32], where the spectra of the single- and double-layer potentials for the Laplace operator were derived. Here we derive the layer operator spectra for a single particle of radius 1.

Let potential ϕ be a solution to the screened Laplace equation with parameter λ. On the surface of a sphere, ϕ may be written as a superposition of spherical harmonics,

so we make the ansatz that

$$\phi = a_n^m f_n(r) Y_n^m(\theta, \phi)$$

for all r. Plugging ϕ into the screened Laplace operator and employing orthogonality of the Y_n^m, we obtain an ODE for $f_n(r)$:

$$r^2 f_n^{''} + 2r f_n^{'} - \left[\lambda^2 r^2 + n(n+1)\right] f_n = 0. \tag{42}$$

This equation is known as the *spherical Bessel differential equation* and has two sets of admissible solutions, called modified spherical Bessel and Hankel functions and denoted respectively by i_n and k_n. These functions can be expressed in terms of modified Bessel functions as:

$$i_n(\lambda r) = \sqrt{\frac{\pi}{2\lambda r}} I_{n+\frac{1}{2}}(\lambda r), \quad k_n(\lambda r) = \sqrt{\frac{\pi}{2\lambda r}} K_{n+\frac{1}{2}}(\lambda r), \tag{43}$$

where $I_n(r)$ is the modified Bessel function of the first kind and $K_n(r)$ is the modified Bessel function of the second kind.

Layer potential

We use our representation of solutions to the screened Laplace equation in conjunction with properties of layer operators to solve for the spectral values of the single- and double-layer operators.

Let $\varphi = \mathcal{S}_\lambda[Y_n^m]$. We have that

$$\varphi(r, \theta, \phi) = \begin{cases} \sum_{n=0}^{\infty} \sum_{m=-n}^{n} a_{nm}^o k_n(\lambda r) Y_n^m(\theta, \phi) & r > 1 \\ \sum_{n=0}^{\infty} \sum_{m=-n}^{n} a_{nm}^i i_n(\lambda r) Y_n^m(\theta, \phi) & r < 1, \end{cases}$$

with $\{a_{nm}^o\}$, $\{a_{nm}^i\}$ unknown coefficients for the exterior and interior respectively. By using the continuity of $\mathcal{S}$ at the boundary and orthogonality of Y_n^m, we obtain an equation relating the coefficients:

$$a_{nm}^o k_n(\lambda) - a_{nm}^i i_n(\lambda) = 0. \tag{44a}$$

the jump condition $[[S'\phi]] = -\phi$ yields a second equation for the coefficients:

$$a_{nm}^o \lambda k_n'(\lambda) - a_{nm}^i \lambda i_n'(\lambda) = -1. \tag{44b}$$

Solving the 2×2 linear system for each pair of (n, m) gives us that:

$$a_{nm}^i = \frac{-k_n(\lambda)}{\lambda\ W\left(i_n(\lambda), k_n(\lambda)\right)}, \quad a_{nm}^o = \frac{-i_n(\lambda)}{\lambda\ W\left(i_n(\lambda), k_n(\lambda)\right)}, \tag{45}$$

where W is the Wronskian

$$W\left(i_n(\lambda), k_n(\lambda)\right) = i_n(\lambda) k_n'(\lambda) - k_n(\lambda) i_n'(\lambda).$$

It can be shown that $W(i_n(\lambda), k_n(\lambda)) = -\dfrac{\pi}{2\lambda^2}$. From this, the values in Theorem 1 follow. A nearly identical analysis yields the double-layer coefficients, with only the jump conditions on the layer operator changing.

Appendix B. Derivatives of operators

The formulas for the kernels of the normal derivatives of the layer operators $\mathcal{S}$ and $\mathcal{D}$ are given below. Here $\boldsymbol{v_x}$ and $\boldsymbol{v_y}$ are the normal vectors evaluated at $\boldsymbol{x}$ and $\boldsymbol{y}$ respectively. Also, let ζ_x denote the dot product $\zeta_x = \boldsymbol{v_x}^T(\boldsymbol{x}-\boldsymbol{y})$, and $\zeta_y = \boldsymbol{v_y}^T(\boldsymbol{x}-\boldsymbol{y})$.

$$\mathcal{S}'_\lambda = \frac{\zeta_x}{4\pi}\frac{e^{-\lambda\|\boldsymbol{x}-\boldsymbol{y}\|}}{\|\boldsymbol{x}-\boldsymbol{y}\|^2}\left(\frac{1}{\|\boldsymbol{x}-\boldsymbol{y}\|}+\lambda\right), \tag{46a}$$

$$\begin{aligned}\mathcal{D}'_\lambda = \frac{e^{-\lambda\|\boldsymbol{x}-\boldsymbol{y}\|}}{4\pi}\Bigg[&\frac{1}{\|\boldsymbol{x}-\boldsymbol{y}\|^3}\left(\lambda^2+\frac{2\lambda}{\|\boldsymbol{x}-\boldsymbol{y}\|}+\frac{2}{\|\boldsymbol{x}-\boldsymbol{y}\|^2}\right)\zeta_x\zeta_y \\ &-\left(\frac{\lambda}{\|\boldsymbol{x}-\boldsymbol{y}\|}+\frac{1}{\|\boldsymbol{x}-\boldsymbol{y}\|^2}\right)\left(\frac{1}{\|\boldsymbol{x}-\boldsymbol{y}\|}(\boldsymbol{v_x}^T\boldsymbol{v_y})-\frac{1}{\|\boldsymbol{x}-\boldsymbol{y}\|^3}\zeta_x\zeta_y\right)\Bigg].\end{aligned} \tag{46b}$$

The spectra of the derivative operators are as follows:

Appendix C. Scaling analysis

Throughout our analysis of the screened Laplace BIOs, we have defined them on the unit sphere. This is sufficient for calculations involving spheres of any size, as the following result holds:

Lemma 2 *Let $\mathcal{S}^r_\lambda$ and $\mathcal{D}^r_\lambda$ be the single- and double-layer operators for the screened Laplace equation on the surface of a sphere of radius r centered at the origin. Then,*

1. $\mathcal{S}^r_\lambda[\mu](\boldsymbol{x}) = r\mathcal{S}_{\lambda r}[\mu](\boldsymbol{x}/r)$,
2. $\mathcal{D}^r_\lambda[\mu](\boldsymbol{x}) = \mathcal{D}_{\lambda r}[\mu](\boldsymbol{x}/r)$,
3. $\mathcal{S}^{r\prime}_\lambda[\mu](\boldsymbol{x}) = \mathcal{S}'_{\lambda r}[\mu](\boldsymbol{x}/r)$,
4. $\mathcal{D}^{r\prime}_\lambda[\mu](\boldsymbol{x}) = \frac{1}{r}\mathcal{D}'_{\lambda r}[\mu](\boldsymbol{x}/r)$.

These properties can easily be verified by a simple change of variables procedure (e.g., $y' = ry$) to the integrals (1a). Given a routine that evaluates the quantities in 1, the above lemma allows for the same quantities to be evaluated on spheres of any size by scaling the input and output and changing parameter λ to λr.

Appendix D. Nondimensionalization

We discuss the nondimensionalization of units in physical applications. In Sections 4 and 5, a natural choice of unit length, L is the Debye length, λ^{-1}.

Amphiphilic Janus particles

In addition to the characteristic length $L = \lambda^{-1}$, we define a characteristic value of the potential, ϕ_c. Prior to nondimensionalization, the hydrophobic stress tensor is given by:

$$T_H = \left(\lambda^2\phi^2 I + 2(\|\nabla\phi\|^2 - \nabla\phi \otimes \nabla\phi)\right). \tag{47}$$

We nondimensionalize this expression by substituting $\frac{\phi}{\phi_c}$ into the tensor, which yields

$$T_H = \frac{\phi_c^2}{L^2} T'_H. \tag{48}$$

$\frac{\phi_c^2}{L^2}$ has units of pressure. We refer to it as the *amphiphilic pressure*, π_a. We follow the standard nondimensionalization of the Stokes equation:

$$T_S = \frac{\mu u_c}{L_c}(-p_c I + \left(\nabla u' + \nabla u'^T\right)) = \pi_v T'_S, \tag{49}$$

where u_c is a characteristic fluid speed and $\pi_v = \frac{\mu u_c}{L}$ is referred to as the *viscous pressure*. Equating the two tensors and dividing through by the viscous pressure, we obtain

$$T_S = \eta T_H,$$

where $\eta = \pi_a/\pi_v$ is the ratio of amphiphilic pressure to viscous pressure.

Bipolar particles

We again let L equal the Debye length. Since we have normalized the exterior screened Laplace equation, $L = 1$. In this case, we use the potential from the electric field to define ϕ in terms of $\|\boldsymbol{E_0}\|L$.. Using these values in the Maxwell stress tensor, we obtain

$$T_E = (\epsilon_0)\|\boldsymbol{E_0}\|^2 \left(\nabla\phi' \times \nabla\phi' - \frac{\|\nabla\phi'\|^2}{2}\right). \tag{50}$$

$\epsilon_0\|\boldsymbol{E_0}\|^2$ is two times the *electrostatic pressure* and may be denoted as π_e. Just like in the amphiphilic case, we can equate this tensor with the Stokes tensor and define η as the ratio between electrostatic and viscous pressures yielding

$$T_S = \eta T_E, \tag{51}$$

where $\eta = \pi_e/\pi_v$.

Phoretic particles

We model phoretic particles with the Laplace equation, so we cannot use a Debye length as the unit length. Rather, we let L be the particle radius.

The concentration is modeled by a diffusion equation:

$$D\nabla^2 C = 0. \tag{52}$$

We set the unit time to be $T = L^{-1/2}$ so that D is dimensionless.

Unlike the amphiphilic and bipolar cases, the key coupling between Janus and hydrodynamic interactions for phoretic particles occurs through the tangential slip velocity induced at particle boundaries. After nondimensionalization, we obtain

$$\boldsymbol{u}_{slip} = \frac{D}{u_c L} M_k(\theta_k)(I - \boldsymbol{n}\boldsymbol{n}^T)\nabla C, \tag{53}$$

where C_c is the unit concentration. The quantity $(D/L)/u_c$ is a ratio between the speed of diffusion and the fluid speed. For all experiments presented in this section, we choose u_c to be the speed of a single phoretic particle in unbounded flow. This characteristic speed may be chosen differently if mean particle velocity deviates significantly from this.

References

1. Yang, Z., Muller, A.H., Xu, C., Doyle, P.S., DeSimone, J.M., Lahann, J., Sciortino, F., Glotzer, S., Hong, L., Aarts, D.A., et al.: Janus particle synthesis, self-assembly and applications. Royal Society of Chemistry (2012)
2. Walther, A., Müller, A.H.: Janus particles. Soft Matter **4**(4), 663–668 (2008)
3. Hong, L., Cacciuto, A., Luijten, E., Granick, S.: Clusters of amphiphilic colloidal spheres. Langmuir **24**, 621–625 (2008)
4. Su, H., Price, C.-A.H., Jing, L., Tian, Q., Liu, J., Qian, K.: Janus particles: design, preparation, and biomedical applications. Materials today bio **4**, 100033 (2019)
5. Yang, S., Guo, F., Kiraly, B., Mao, X., Lu, M., Leong, K.W., Huang, T.J.: Microfluidic synthesis of multifunctional janus particles for biomedical applications. Lab on a Chip **12**(12), 2097–2102 (2012)
6. Patra, D., Sengupta, S., Duan, W., Zhang, H., Pavlick, R., Sen, A.: Intelligent, self-powered, drug delivery systems. Nanoscale **5**(4), 1273–1283 (2013)
7. Fu, S.-P.P., Ryham, R., Klöckner, A., Wala, M., Jiang, S., Young, Y.-N.: Simulation of multiscale hydrophobic lipid dynamics via efficient integral equation methods. Multiscale Modeling & Simulation **18**(1), 79–103 (2020)
8. Fu, S.-P., Quaife, B., Ryham, R., Young, Y.-N.: Two-dimensional hydrodynamics of a janus particle vesicle. Journal of Fluid Mechanics 941 (2022)
9. Kanso, E., Michelin, S.: Phoretic and hydrodynamic interactions of weakly confined autophoretic particles. The Journal of Chemical Physics **150**(4), 044902 (2019)
10. Kim, H.E., Kim, K., Ma, T.Y., Kang, T.G.: Numerical investigation of the dynamics of janus magnetic particles in a rotating magnetic field. Korea-Australia Rheology Journal **29**(1), 17–27 (2017)
11. Sobecki, C., Zhang, J., Wang, C.: Dynamics of a pair of paramagnetic janus particles under a uniform magnetic field and simple shear flow. Magnetochemistry **7**(1), 16 (2021)
12. Daghighi, Y., Gao, Y., Li, D.: 3d numerical study of induced-charge electrokinetic motion of heterogeneous particle in a microchannel. Electrochimica Acta **56**(11), 4254–4262 (2011)
13. Molotilin, T.Y., Lobaskin, V., Vinogradova, O.I.: Electrophoresis of janus particles: A molecular dynamics simulation study. The Journal of Chemical Physics **145**(24), 244704 (2016)
14. Baran, Ł, Borówko, M., Rżysko, W.: Self-assembly of amphiphilic janus particles confined between two solid surfaces. The Journal of Physical Chemistry C **124**(32), 17556–17565 (2020)
15. Banik, M., Sett, S., Bakli, C., Raychaudhuri, A.K., Chakraborty, S., Mukherjee, R.: Substrate wettability guided oriented self assembly of janus particles. Scientific Reports **11**(1), 1–8 (2021)
16. Wajnryb, E., Mizerski, K.A., Zuk, P.J., Szymczak, P.: Generalization of the rotne-prager-yamakawa mobility and shear disturbance tensors. Journal of Fluid Mechanics 731 (2013)
17. Brady, J.F., Bossis, G.: Stokesian dynamics. Annual Review of Fluid Mechanics **20**(1), 111–157 (1988)
18. Cichocki, B., Felderhof, B.U., Hinsen, K., Wajnryb, E., Bławzdziewicz, J.: Friction and mobility of many spheres in stokes flow. The Journal of Chemical Physics **100**(5), 3780–3790 (1994)
19. Maxey, M.: Simulation methods for particulate flows and concentrated suspensions. Annual Review of Fluid Mechanics **49**, 171–193 (2017)

20. Rahimian, A., Lashuk, I., Veerapaneni, S., Chandramowlishwaran, A., Malhotra, D., Moon, L., Sampath, R., Shringarpure, A., Vetter, J., Vuduc, R., et al.: Petascale direct numerical simulation of blood flow on 200k cores and heterogeneous architectures. In: SC'10: Proceedings of the 2010 ACM/IEEE International Conference for High Performance Computing, Networking, Storage and Analysis, pp. 1–11 (2010). IEEE
21. Malhotra, D., Biros, G.: Pvfmm: A parallel kernel independent fmm for particle and volume potentials. Communications in Computational Physics **18**(3), 808–830 (2015)
22. Lu, L., Rahimian, A., Zorin, D.: Parallel contact-aware simulations of deformable particles in 3d stokes flow. arXiv preprint arXiv:1812.04719 (2018)
23. Yan, W., Corona, E., Malhotra, D., Veerapaneni, S., Shelley, M.: A scalable computational platform for particulate stokes suspensions. Journal of Computational Physics **416**, 109524 (2020)
24. Corona, E., Veerapaneni, S.: Boundary integral equation analysis for suspension of spheres in stokes flow. Journal of Computational Physics **362**, 327–345 (2018)
25. Corona, E., Greengard, L., Rachh, M., Veerapaneni, S.: An integral equation formulation for rigid bodies in stokes flow in three dimensions. Journal of Computational Physics **332**, 504–519 (2017)
26. Rosenthal, G., Klapp, S.H.: Micelle and bilayer formation of amphiphilic janus particles in a slit-pore. International Journal of Molecular Sciences **13**(8), 9431–9446 (2012)
27. Katuri, J., Ma, X., Stanton, M.M., Sanchez, S.: Designing micro-and nanoswimmers for specific applications. Accounts of Chemical Research **50**(1), 2–11 (2017)
28. Brebbia, C.A., Telles, J.C.F., Wrobel, L.C.: Boundary element techniques: theory and applications in engineering. Springer Science & Business Media (2012)
29. Kress, R., Maz'ya, V., Kozlov, V.: Linear integral equations. Springer 82 (1989)
30. Power, H., Miranda, G.: Second kind integral equation formulation of stokes' flows past a particle of arbitrary shape. SIAM Journal on Applied Mathematics **47**(4), 689–698 (1987)
31. Veerapaneni, S.K., Rahimian, A., Biros, G., Zorin, D.: A fast algorithm for simulating vesicle flows in three dimensions. Journal of Computational Physics **230**(14), 5610–5634 (2011)
32. Vico, F., Greengard, L., Gimbutas, Z.: Boundary integral equation analysis on the sphere. Numerische Mathematik **128**(3), 463–487 (2014)
33. Gimbutas, Z., Veerapaneni, S.: A fast algorithm for spherical grid rotations and its application to singular quadrature. SIAM Journal on Scientific Computing **35**(6), 2738–2751 (2013)
34. Greengard, L., Rokhlin, V.: A fast algorithm for particle simulations. Journal of Computational Physics **73**(2), 325–348 (1987)
35. Greengard, L.F., Huang, J.: A new version of the fast multipole method for screened coulomb interactions in three dimensions. Journal of Computational Physics **180**(2), 642–658 (2002)
36. Gimbutas, Z., Greengard, L.: STKFMMLIB3D 1.2. https://cims.nyu.edu/cmcl/cmcl.html (2012)
37. Gimbutas, Z., Greengard, L.: STFMMLIB3-Fast Multipole Method (FMM) library for the evaluation of potential fields governed by the Stokes equations in R3 (2012)
38. Greengard, L., Gimbutas, Z.: FMMLIB3D (2012)
39. Mohlenkamp, M.J.: A fast transform for spherical harmonics. Journal of Fourier analysis and applications **5**(2–3), 159–184 (1999)
40. Fletcher, R.: Optimization and control with applications: On the barzilai-borwein method. Springer, 235–256 (2005)
41. Marčelja, S., Mitchell, D.J., Ninham, B.W., Sculley, M.J.: Role of solvent structure in solution theory. Journal of the Chemical Society, Faraday Transactions 2: Molecular and Chemical Physics 73(5), 630–648 (1977)
42. Eriksson, J.C., Ljunggren, S., Claesson, P.M.: A phenomenological theory of long-range hydrophobic attraction forces based on a square-gradient variational approach. Journal of the Chemical Society, Faraday Transactions 2: Molecular and Chemical Physics 85(3), 163–176 (1989)
43. Ryham, R.J., Klotz, T.S., Yao, L., Cohen, F.S.: Calculating transition energy barriers and characterizing activation states for steps of fusion. Biophysical journal **110**(5), 1110–1124 (2016)
44. Zhang, J., Grzybowski, B.A., Granick, S.: Janus particle synthesis, assembly, and application. Langmuir **33**(28), 6964–6977 (2017)
45. Pawar, A.B., Kretzschmar, I.: Fabrication, assembly, and application of patchy particles. Macromolecular rapid communications **31**(2), 150–168 (2010)
46. Velev, O.D., Gangwal, S., Petsev, D.N.: Particle-localized ac and dc manipulation and electrokinetics. Annual Reports Section" C"(Physical Chemistry) 105, 213–246 (2009)

47. Seong, Y., Kang, T.G., Hulsen, M.A., den Toonder, J.M., Anderson, P.D.: Magnetic interaction of janus magnetic particles suspended in a viscous fluid. Physical Review E **93**(2), 022607 (2016)
48. Hossan, M.R., Gopmandal, P.P., Dillon, R., Dutta, P.: Bipolar janus particle assembly in microdevice. Electrophoresis **36**(5), 722–730 (2015)
49. Gilson, M.K., Davis, M.E., Luty, B.A., McCammon, J.A.: Computation of electrostatic forces on solvated molecules using the poisson-boltzmann equation. The Journal of Physical Chemistry **97**(14), 3591–3600 (1993)
50. Geng, W., Krasny, R.: A treecode-accelerated boundary integral poisson-boltzmann solver for electrostatics of solvated biomolecules. Journal of Computational Physics **247**, 62–78 (2013)
51. Juffer, A., Botta, E.F., van Keulen, B.A., van der Ploeg, A., Berendsen, H.J.: The electric potential of a macromolecule in a solvent: A fundamental approach. Journal of Computational Physics **97**(1), 144–171 (1991)
52. Golestanian, R., Liverpool, T., Ajdari, A.: Designing phoretic micro-and nano-swimmers. New Journal of Physics **9**(5), 126 (2007)